Check for updates

View Article Online
View Journal

Nanoscale

Accepted Manuscript

This article can be cited before page numbers have been issued, to do this please use: V. Rodriguez-Fajardo, V. Sanz, I. De Miguel, J. Berthelot, S. Aimovi, R. Porcar-Guezenec and R. Quidant, *Nanoscale*, 2018, DOI: 10.1039/C7NR09408F.

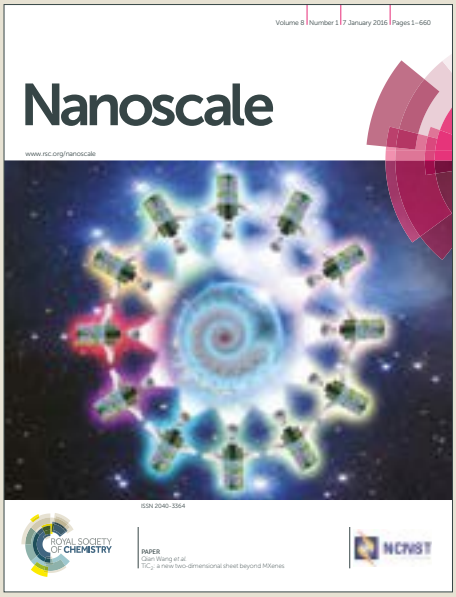

This is an Accepted Manuscript, which has been through the Royal Society of Chemistry peer review process and has been accepted for publication.

Accepted Manuscripts are published online shortly after acceptance, before technical editing, formatting and proof reading. Using this free service, authors can make their results available to the community, in citable form, before we publish the edited article. We will replace this Accepted Manuscript with the edited and formatted Advance Article as soon as it is available.

You can find more information about Accepted Manuscripts in the author guidelines.

Please note that technical editing may introduce minor changes to the text and/or graphics, which may alter content. The journal's standard Terms & Conditions and the ethical guidelines, outlined in our author and reviewer resource centre, still apply. In no event shall the Royal Society of Chemistry be held responsible for any errors or omissions in this Accepted Manuscript or any consequences arising from the use of any information it contains.

ROYAL SOCIETY OF CHEMISTRY

rsc.li/nanoscale

View Article Online
DOI: 10.1039/C7NR09408F
ROYAL SOCIETY OF CHEMISTRY

Journal Name

ARTICLE TYPE

Cite this: DOI: 10.1039/xxxxxxxxxx

Two-Color Dark-Field (TCDF) microscopy for metal nanoparticles imaging inside cells†

Valeria Rodríguez-Fajardo,[a,b] Vanesa Sanz,[a] Ignacio de Miguel,[a] Johann Berthelot,[a‡] Srdjan S. Aćimović,[a§] Rafael Porcar-Guezenec,[b] and Romain Quidant*[a,c]

Received Date
Accepted Date

DOI: 10.1039/xxxxxxxxxx

www.rsc.org/journalname

Noble metal nanoparticles (NPs) supporting localized surface plasmon resonances are widely used in the context of biotechnology as optical and absorption contrast agents with great potential applicability to both diagnostics and less invasive therapies. In this framework, it is crucial to have access to simple and reliable microscopy techniques to monitor the NPs that have internalized into cells. While dark field (DF) microscopy takes advantage of the enhanced NPs scattering at their plasmon resonance, its use in cells is limited by the large scattering background from the internal cell compartments. Here, we report on a novel two-color dark field microscopy that addresses these limitations by significantly reducing the cell scattering contribution. We first present the technique and demonstrate its enhanced contrast, specificity and reliability for NP detection compared to standard optical dark field. We then demonstrate its potential suitability in two different settings, namely wide-field parallel screening of circulating cells in microfluidic chip and high-resolution tracking of internalized NPs in cells. These proof of principle experiments show a promising capability of this approach with possible extension to other kinds of targeted systems like bacteria and vesicles.

Nanotechnology has emerged as one of the most promising enabling technologies with applications to very diverse fields. Among the most appealing applications is medicine[1,2], where nanoparticles can be used for on-a-chip biosensing[3,4], early diagnosis[5–7] and less invasive and more efficient treatments of diseases[8–10]. Within the plethora of available materials, gold nanoparticles (AuNPs) have attracted significant interest owing to a unique set of properties including biocompatibility, well-studied surface functionalization for targeting, tunability of its optical properties and, particularly, because they can be used as theranostic agents, for both diagnosis and treatment[11–17]. In order to fully take advantage of their benefits, it is first necessary to comprehensively explore the interaction between metal NPs and cells including uptake, toxicity and fate of the NPs after internalization. This is not always an easy task since such interaction depends on a very broad variety of factors including, but not limited to, NPs shape, composition, surface chemistry, cell type, and culture medium[18–26]. Therefore, the ability of reliably and quickly detect NPs is crucial for studying such an interaction in real time. In addition, fast and accurate NP identification could potentially allow for efficient population differentiation.

Several techniques can be used to image metal AuNPs inside cells, being electron microscopy (SEM/TEM), two-photon luminescence (TPL) and dark-field (DF) microscopy the most commonly used[12,27–32]. While electron microscopy outperforms in terms of resolution and therefore localization of NPs, it requires extensive sample preparation and is highly invasive. TPL is inherently a nonlinear confocal microscopy method that exploits the luminescence of gold upon the absorption of two photons[33,34] to spot NPs inside the cells with good accuracy. Because the two-photon induced self-luminescence of cells is negligible, the contrast of gold NPs is very high. However, high peak powers of pulsed illumination can alter the NPs geometry and consequently the measurements. Moreover, these techniques require complex and expensive equipment, and are unable to have sufficient temporal resolution to follow the NP-cell interaction dynamics or track cells in flowing conditions.

In this context, DF microscopy stands out as a great alternative, as it is simple, fast, cheap, non-invasive, and does not suffer blinking or bleaching. However, since the scattering of the cell it-

[a] ICFO-Institut de Ciencies Fotoniques, The Barcelona Institute of Science and Technology, 08860 Castelldefels, Barcelona, Spain; E-mail: romain.quidant@icfo.eu
[b] COSINGO-Imagine Optic Spain S.L., Av. Canal Olimpic, s/n 08860 Castelldefels (Barcelona) Spain.
[c] ICREA-Institució Catalana de Recerca i Estudis Avançats, 08010 Barcelona, Spain.
‡ Present address: Aix Marseille Université, CNRS, Centrale Marseille, Institut Fresnel UMR 7249, 13397 Marseille, France.
§ Present address: NIL Technology ApS, Diplomvej 381, DK-2800 Kongens Lyngby, Denmark.
† Electronic Supplementary Information (ESI) available: Supporting additional data. See DOI: 10.1039/b000000x/

Published on 17 January 2018. Downloaded by University of Reading on 19/01/2018 20:21:25.

Nanoscale Accepted Manuscript

View Article Online
DOI: 10.1039/C7NR09408F

Published on 17 January 2018. Downloaded by University of Reading on 19/01/2018 20:21:25.

self can be very high, DF alone is not reliable for detecting metal NPs embedded in cells[35,36]. Moreover, it is impractical to carry out a constant background subtraction because the cell's scattering can significantly vary from individual to individual, or within different cell compartments[37,38]. Several approaches have been proposed to overcome this issue, both from the optical and cellular perspectives. For instance, Cui *et al.* developed a chemical method that reduces the scattering from the cells, thus improving the images signal-to-noise-ratio[39]. However, this technique is incompatible with live cell studies. On the other hand, Cytoviva, Inc. has tackled the problem by acquiring scattering spectra in addition to the DF images[40]. Similarly, hyperspectral imaging has also been explored[41], yet these last two approaches critically suffer from speed limitations.

The use of multi-color dark-field microscopy has been employed in the context of the so-called plasmon ruler[42,43]. In this case, the shift in the plasmon resonance due to the proximity of two nanoparticles is used to measure the distance between cells' complexes with sub-diffraction accuracy and high temporal resolution. However, it is only suitable when the scattering background is low, which is often not the case for living cells[44].

Here, we present a novel two-color DF (TCDF) imaging technique that circumvents the limitations of standard DF microscopy, offering an enhanced contrast and specificity to map resonant plasmonic nanoparticles in samples with high scattering power like cells. Our method has several important advantages over others: its acquisition speed is not fundamentally limited; it is harmless for the cells and; does not suffer from artefacts of scanning methods when studying living specimens. These features result in great potential for high-throughput screening and tracking of fast dynamics of metal NPs in cells. In this paper, we first describe the general concept of TCDF and provide the experimental details for its implementation, followed by an analysis of its performance over standard DF in terms of discrimination capacity and sensitivity. Finally, we report proof of principle experiments towards both wide-field cell screening in flow and high-resolution detection of metal NPs.

Experimental details

Method description

Our method relies on the fact that the spectral optical response of metal NPs and cells strongly differ. Light scattering by metal NPs depends strongly on the incident wavelength, showing a maximum at their localized plasmon resonance[12,45]. Conversely, the scattering of cells depends weakly on wavelength (Supplementary information figure S1). This difference is exploited to isolate the NPs scattering from the one of the cells by using differential imaging at two different wavelengths. Since our technique uses scattering, it is robust, non-invasive, and only requires a simple set-up. Importantly, its temporal resolution only depends on the camera speed and intensity of light sources, because the scattering intensity is not restricted by a limited photon budget.

Figure 1 sketches the working principle of TCDF. For illustration purposes, here we show a sample consisting of three neighbouring cells, two loaded with gold nanoparticles (left), the other one without NPs (right). The sample is illuminated simultaneously with two wavelengths; one coinciding with the plasmon resonance of the metal NPs ($\lambda_{on} = 780$ nm), the other one off-resonance ($\lambda_{off} = 590$ nm). Light on-resonance is scattered both by the cells and the metal NPs, whereas light off-resonance gets predominantly scattered only by the cells. The scattered light from each illumination channel is detected in separate cameras simultaneously, leading to two monochromatic images. Given that scattered light by cells is nearly identical for both wavelengths, an image subtraction enables us to separate the NPs' scattering. Therefore, cells without NPs will vanish in the image subtraction, highlighting the decorated ones.

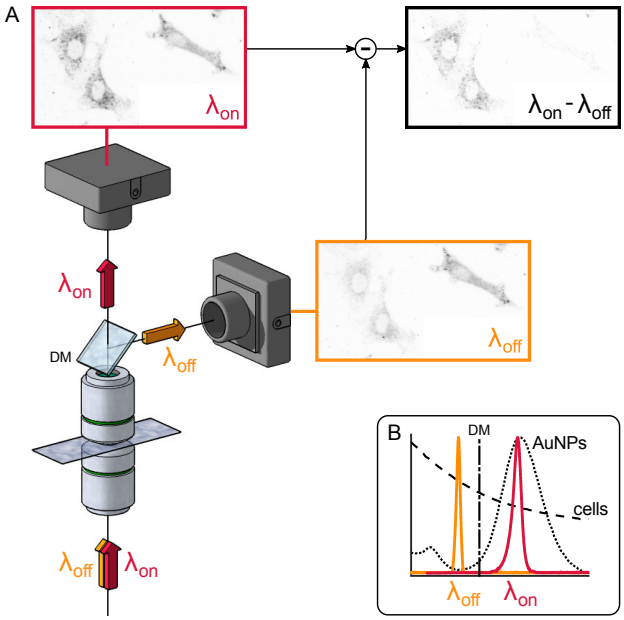

Fig. 1 TCDF concept. A. Cells with or without metal NPs are illuminated simultaneously with two wavelengths: one resonant with the plasmon peak (λ_{on}, in red) and the other off-resonance (λ_{off}, in orange). Two monochromatic images corresponding to each illumination wavelength are independently acquired, and subsequently subtracted. Since both images share the scattering information of the cells but only one (the on-resonance image) contains information of the resonant scattering of the NPs, the image subtraction isolates the optical response of the NPs. **B.** We also show, for reference, real emission spectra of the lamps used (orange and red curves) against the scattering spectra of both AuNPs and cells (dotted and dashed lines, respectively), as well as the cutoff wavelength of the dichroic mirror used (dashed-dotted line).

Optical set-up

Light from two diode lamps (Thorlabs, M590L3-C1 and M780L3-C1) was directed towards a dark-field optical condenser (Olympus U-DCW, NA 1.4-1.2) following Köhler illumination scheme. Forward-scattered light from the sample was collected using either a 20x (Olympus UMPLFLN20xW, NA 0.5, water dipping immersion) or a 60x (Nikon CFI Fluor 60x, NA 1, water dipping immersion) microscope objective. Collected light was focused using a 15 cm focal length lens and then separated using a dichroic mirror (Thorlabs DMLP650R) onto two cameras (Pixelink, PL-

Nanoscale Accepted Manuscript

This journal is © The Royal Society of Chemistry [year]

View Article Online
DOI: 10.1039/C7NR09408F

Published on 17 January 2018. Downloaded by University of Reading on 19/01/2018 20:21:25.

B741E).

Lamps wavelengths were chosen to match the off- and on-resonance condition of the used AuNPs. Light sources were unpolarized, so that the orientation of the AuNPs inside the cell is not relevant. Images were acquired using a custom made LabView code, and the cameras were triggered simultaneously using an Arduino. DF images correspond to images acquired at 780 nm. Ultimately, for sake of a better visualization, the image contrast is inverted in a way the AuNPs appear dark on a white background. Images taken with the 20x microscope objective (Discrimination, sensitivity and screening experiments) had an effective magnification of M=17.4, pixel size of 385 nm, and exposure time of 25 ms. Images taken with the 60x objective (High-resolution experiments) had an effective magnification of M=45.6, pixel size of 147 nm, and exposure time of 30 ms.

There are several aspects to consider in order to ensure an optimum implementation of TCDF with reduced uncertainty. First, since scattering is angle-dependent, the illumination pattern with both wavelengths should be as similar as possible. Second, power of light sources should be adjusted to level out the scattering intensities at both wavelengths for control samples. Third, it is fundamental to guarantee both the field of view and the state of focus of the images to be identical, so that the images match with each other spatially. In addition to optical alignment, this can be accomplished digitally by implementing an image registration algorithm. The sensitivity of our method is limited principally by the residual intensity after subtraction of on- and off-resonance images of bare cells. This depends on the previously mentioned experimental aspects, but it is also fundamentally affected by small deviations of the ratio between scattering intensities at the two wavelengths from the average one (Supplementary information figure S1).

TPL imaging

We employed a commercial microscope Leica TCS SP5 using the multifunctional port for IR fs excitation. The IR source was a Ti:Sa MIRA900 laser (Coherent) with 150 fs pulse duration and pumped by a 6W Verdi laser (Coherent). For discrimination, sensitivity and screening experiments, we used a 10x microscope objective (Leica, HCX PL APO CS 10.0x, NA 0.40) and 3.5 mW power at the sample plane. For high-resolution imaging we used a 63x objective (Leica, HCX PL APO CS 63.0x, NA 1.40, oil immersion) and 0.5 mW power.

Image processing

On- and off-resonance images were calibrated prior to subtraction. First, uneven illumination was corrected using a calibration image (acquired using a sample whose structure is invariable over all the field of view). Second, any possible mismatch between the images' field of view was corrected using an image registration algorithm. Cell segmentation was implemented on the off-resonance image using thresholding and morphological operations. Mean intensity was calculated as the average value of the intensity of pixels within the segmented cell. All image processing was carried out using custom made MatLab scripts.

AuNPs

Gold nanorods (GNRs) were synthesized using the seed-mediated method[46,47] to obtain CTAB-caped rods with an aspect ratio of 3.9 and long-axis length of 44 nm. Their longitudinal resonance is centered near 810 nm, and their calculated scattering cross-section about 1×10^{-17} m^2 (Calculation performed using DDScat 7.3[48]). Resonance of the GNRs was tuned within the biological window to reduce the risk of photodamage and maximize the scattering collected. Later, GNRs were incubated overnight with SH-PEG-COOH (alpha-Thio-omega-carboxy poly(ethylene glycol)) to replace the CTAB coating for a PEG one. Then, GNRs were incubated overnight with RGD (Gly-Arg-Gly-Asp-Ser) after activation using Sulfo-NHS (N-Hydroxysulfosuccinimide sodium salt) and EDC (N-(3-Dimethylaminopropyl)-N'-ethylcarbodiimide hydrochloride). Finally, functionalized GNRs were sterilized using a 0.2 um pore filter.

Cells culture and preparation

Cell line A549 was grown in a CO_2 incubator (37° C, 5% CO_2, 90% humidity) in 25 cm^2 flasks using DMEM (Gibco, 21063029) supplemented with 10% FBS (Gibco, 10270). Preparation of cells for experiments consisted in three basic steps: first, cells were seeded at known concentration in 10% FBS-DMEM and incubated for 1 day; second, cells were washed two times with DMEM and incubated overnight in DMEM containing a specific concentration of RGD-functionalized GNRs; and third, cells were washed two times with PBS.

For discrimination and high-resolution experiments (Figures 2 and 5) 5×10^4 cells were seeded in grid glass-bottom petri dishes (Ibidi, 81166). GNRs concentrations were 1 nM and 2 nM for specificity and high-resolution experiments respectively. Experiments for sensitivity measurements with adherent cells (Figure 3A) were carried out using a slide with small wells (Ibidi, 81506), where we seeded 0.3×10^4 cells per well and varied the GNRs concentration from 0 to 4 nM. For this three experiments, cells were prefixed in 2% PFA for 5 min, washed two times with PBS and fixed with 2% PFA for 15 min.

Cells for screening experiments were seeded in glass-bottom petri dishes (Cellvis, D35-20-0-N) at a concentration of 15×10^4 cells per dish and GNRs-concentration according to the specific needs. In this case, cells were detached from culture dish incubating with Trypsin (Biowest, L0940) during 4 minutes at 37° Celsius and the process was blocked with 10%-FBS supplemented DMEM. Cells were resuspended in Live Cell Imaging Solution (Gibco, A14291DJ) for imaging. We used glass-bottom petri dishes for measurements under static conditions (Sensitivity and screening) and a home made microfluidic chip for screening under flowing conditions.

Microfluidic chip

Optical systems utilizing high-NA components (objectives and condensers) typically suffer space restrictions due to associated short working distances (in the range of 150μm) and/or complications imposed by the requirement of the immersion liquid. To surpass such limitations, we engineered a special sort of PDMS-

Nanoscale Accepted Manuscript

View Article Online
DOI: 10.1039/C7NR09408F

Published on 17 January 2018. Downloaded by University of Reading on 19/01/2018 20:21:25.

based microfluidic devices for an up-right based microscope operating in dark-field transmission mode with arbitrary dark-field condenser. The cell consists of thin-membrane (ca. 150μm) with embedded flow-through channels covering the supporting glass slide and bulky PDMS parts on the membrane border, with the aim to provide inlets and outlets as well as to facilitate membrane transfer from the mold to the glass. Channels cross section was 150×75 μm^2 to allow the smooth flow of the cells. The mold was created via photolithography in thick SU8, spincoated multiple times to the final thickness of 75μm. Such mold was pre-passivated by TMCS (three-methyl chloro silane) and Sylgrad 184 PDMS (20:1 ratio of base:curing agent) was spincoated to the final thickness of ca. 150 μm. On the clean, TMCS passivated silicon wafer we poured 5:1 PDMS till the thickness of 5 mm. Both molds were baked at 80° Celsius in the oven for 30 min. Thicker PDMS layer was peeled off the mold, cut into corresponding blocks of $24 \times 7 \times 5$ mm^3, and aligned over the sides of thin-membrane frame, and returned into the oven for additional hour an a half. Once two PDMS blocks got bonded with the PDMS membrane, the later was cut, and was removed off the mold with the help of the PDMS blocks. The inlets/outlets were carefully punched through the bulky PDMS pieces, aligned with the membrane channel ends. The PDMS system (membrane and 2 blocks) was carefully rolled-onto the glass support (75×25 mm^2), and baked overnight. The microfluidic chip used in the screening experiment in flow conditions consisted of 8 parallel isolated channels.

Results

Discrimination accuracy

We start by testing the performance of our method in discriminating between AuNPs-loaded and control cells. To this end, we image the same cells with three different methods (TPL, DF and TCDF) and compare their results on two sets of samples; one where the cells have been incubated with gold nanoparticles (AuNPs) and another with bare cells (control).

Figure 2 presents example images for both control (A, D, G) and AuNPs-loaded cells (B, E, H) for the three different acquisition methods. TPL imaging acts as our reference, showing an excellent contrast between the two cells (A vs. B). While standard DF gives very similar intensity levels (D vs E), an equivocal distinction is achieved with TCDF (G vs H). This behaviour is highly repeatable as demonstrated by the histograms shown in Figure 2 (C, F, I), where we present distributions of the mean intensity for both control (N=35) and AuNP-loaded (N=50) cells. Because bare cells show negligible TPL signal, the separation between the two distributions appears very sharp (C). On the contrary, distribution of mean intensities for control sample in DF is very broad, making it impossible to discern unequivocally between cell populations (F). Using TCDF, the distribution of control sample is much narrower, thus dramatically increasing the contrast between control and AuNPs-loaded cells (I).

Sensitivity

Beyond its improved reliability to discriminate AuNPs-loaded from bare cells, another important feature about our method in comparison with standard DF microscopy is the improved sensitivity, understood as the minimum amount of AuNPs that the method is able to identify. Figure 3 presents the contrast between cells with AuNPs and control cells for different AuNPs concentrations during incubation, both for adherent (A) and suspension (B) cells. Solid lines correspond to fitting to a Hill equation of the mean values, a model that is routinely used in biochemistry to describe the binding of a ligand to a macromolecule. Coloured areas represent the standard deviation. For each concentration, we compute the contrast C as

$$C = \frac{\langle \bar{I} \rangle - \langle \bar{I}_0 \rangle}{\sigma_0},$$

where $\bar{I}$ is the mean intensity of one cell, $\langle\rangle$ the average and σ the standard deviation of the sample (over all analysed cells) and the subscript 0 refers to the control sample (No AuNPs during incubation). For each method, we established a threshold using the control sample, defined as its average mean intensity value plus two times its standard deviation (Supplementary figure S3). Moreover, we quantify the method's sensitivity as the AuNPs concentration whose fitted contrast value is equal to such a threshold, or in other words, as the minimum value of AuNPs concentration that allows for clear discrimination of AuNPs-loaded cells.

Data shown for adherent cells (Figure 3A) are the result of four independent realizations of the experiment. One first observes that the contrast is always higher with TCDF than with DF and that DF contrast scarcely reaches the threshold. We compute a sensitivity of 0.52 nM for TCDF, whereas for DF the fitted curve remains below threshold independently of the AuNPs concentration. It is also relevant to highlight that TCDF contrast curves follow the same trend for AuNPs uptake reported in the literature, i.e. it increases with NPs concentration until reaching a plateau[20,27,49]. In the case of suspension cells (Figure 3B), although shaded regions slightly overlap, the contrast is also always higher for TCDF than for DF. Here, measured sensitivity is 0.55 nM and 0.19 nM for DF and TCDF, respectively, what evinces an increase of 2.9 fold. Sensitivity values for TCDF prove its applicability to biological research as typical concentrations used are in the range of nM. Interestingly, contrast values are higher for both DF and TCDF compared to the ones of adherent cells. This can be explained by realizing suspension cells fill a smaller area on the image, resulting in higher effective AuNPs concentration.

Potential applications

Screening of specific specimens in mixed populations is of great importance in medicine[31,50–52]. For instance, AuNPs can be used for targeting circulating tumor cells (CTCs), which play a significant role in the assessment of metastasis risk and cancer treatment prognosis, and whose identification is very challenging because they are very rare in large population of healthy cells[11,53–56]. In this context, AuNPs can be used as stable and bright contrast agents for targeting specific protein markers at

Nanoscale Accepted Manuscript

This journal is © The Royal Society of Chemistry [year]

View Article Online
DOI: 10.1039/C7NR09408F

Published on 17 January 2018. Downloaded by University of Reading on 19/01/2018 20:21:25.

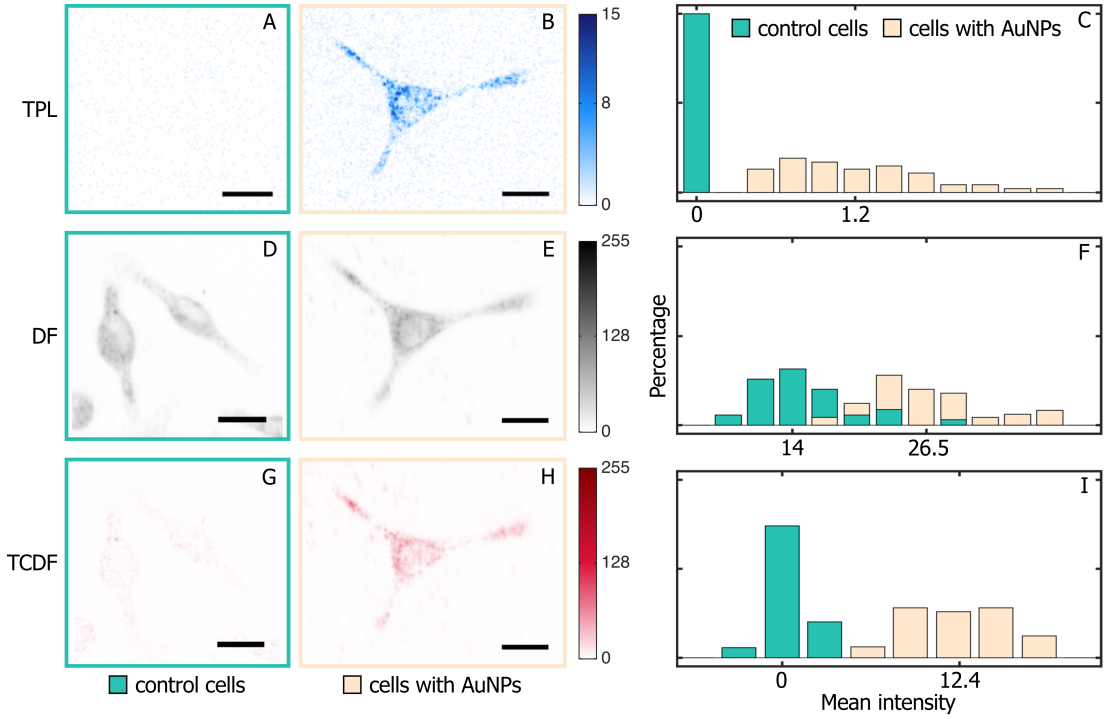

Fig. 2 Unequivocal discrimination between AuNPs-loaded and control cells using TCDF microscopy. Selection of images of control (A, D, G) and AuNPs-loaded (B, E, H) cells for TPL (A, B), DF (D, E) and TCDF (G, H). Scale bar is 20 μm. Images shown exemplify that while contrast between control and AuNPs cells is very high for TPL (A vs. B) and TCDF (G vs. H), no clear distinction is possible with standard DF (D vs. E). Images for each wavelength of cells shown are presented in supplementary figure S2. Histograms of mean intensity (C, F, I) showing the same behavior over a large number of cells (Control and AuNPs distributions in green and light orange, respectively). We analyzed 35 and 50 cells for control and AuNPs samples, respectively, and plot the percentage of cells per sample within a specific mean intensity range. Histograms were computed for the same set of cells for the three methods. Two photon luminescence (TPL) allows for unequivocal discrimination of cells loaded or not with AuNPs (C). Dark-field (DF) does not because the control distribution is very broad and overlaps with the AuNPs distribution (F). By using two-color Dark-field (TCDF) we make the control distribution narrower and diminish the overlap between distributions considerably, therefore allowing for a much clearer discrimination between both cell populations (I).

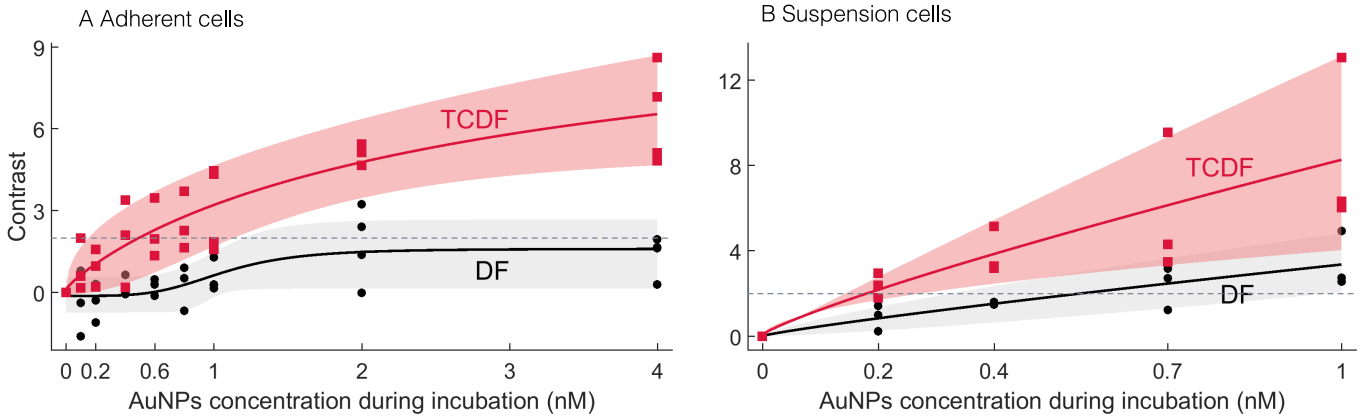

Fig. 3 Enhanced contrast of TCDF microscopy for both adherent (A) and suspension (B) cells. Data shown correspond to 4 and 3 independent realizations for adherent and suspension cells, respectively. Mean values were fitted to a Hill model. Contrast is always higher for TCDF than for standard DF in both cases, confirming our approach performs much better than DF for identifying metal NPs inside cells. Sensitivity in each case was calculated as the concentration value for which the contrast value of the fitted curve is 2, which we established as the threshold for distinguish cells loaded with AuNPs from bare cells. We found values of 0.52 nM for TCDF in the first case (A), and 0.55 nM and 0.19 nM for DF and TCDF respectively in the second (B). Sensitivity values establish the minimum amount of NPs that the method is able to identify. Importantly, the sensitivity is higher for TCDF irrespective of the cell's morphology.

Nanoscale Accepted Manuscript

View Article Online
DOI: 10.1039/C7NR09408F

Published on 17 January 2018. Downloaded by University of Reading on 19/01/2018 20:21:25.

the cell membrane.

Figure 4 presents the results for population differentiation of suspension cells loaded with AuNPs versus bare suspension cells, under both static and flowing conditions. We compare the performance of TCDF against standard DF, using TPL as a reference. For each method, we established a threshold using the control sample, defined as its mean intensity value plus its standard deviation (Supplementary figure S4). We then classified the cells, in such a way a cell with intensity lower than the threshold is considered not to have AuNPs. Conversely, a cell with intensity above the threshold is considered as loaded with NPs. While figure 4 shows results only for suspension cells, TCDF could be easily applied to screening of adherent cells, as can be inferred from discrimination and sensitivity experiments.

Three different samples were measured: AuNPs-loaded and control cells, as well as an equal mixture of both populations. For each sample-imaging method combination, we plot the reconstructed proportion of bare/AuNPs-loaded cells based on the analysis over N cells (N appears on top of each of the result bars). TPL data agree perfectly with the intended proportions, hence ruling out any substantial uncertainty associated to the sample preparation.

Figure 4A summarizes the data obtained under static conditions. It is shown that conventional DF strongly underestimates the number of cells decorated with AuNPs, leading to a very large uncertainty that is inappropriate to reliably differentiate both populations. The differentiation accuracy is dramatically increased by the TCDF approach. As an illustration, the error is reduced from 27% with DF to 5% with TCDF for the mixed sample. Discrepancy between TCDF and TPL arise from the current sensitivity of TCDF and the variability in the NPs uptake within the cell's population. TPL distribution of intensity values for control samples is very narrow (as in Figure 2C) in a way even low concentrations of nanoparticles are easily distinguishable. TCDF's wider distribution is such that cells with few AuNPs are not identified as loaded.

At that stage, it is relevant to test the compatibility of TCDF for cell screening under flowing conditions with the aim to increase the number of processed cells per unit of time. To this aim, we developed a dedicated ultra-thin microfluidic chip, compatible with the short working distance of the dark-field condenser and detection objective (see section 1). Results, shown in figure 4B, demonstrate flow conditions do not alter the accuracy of TCDF measurements. While we do not aim here, with this proof of principle, to outperform flow cytometry, the combination of flow and wide field imaging may be an asset to be further studied.

Another very valuable feature of the method is the potential for assessing NPs-cells interaction at the single cell level, e.g. by determining how long it takes to the NPs to get inside the cell, their location and/or their clearance from the cell. Long term imaging with our method is possible because it is not harmful for the cells (Supplementary Figure S6) and does not affect the metal NPs (Supplementary Figure S7). TCDF has also real-time capabilities, since how fast the images can be acquired depends only on camera speed and light sources intensity.

Figure 5 displays an example of high-resolution images of a cell loaded with AuNPs obtained with the three different methods. For this specific experiment, cells were fixed, so the different methods can be compared directly on the same specimen. A, C and E show the complete cell, and B, D and F an enlarged area of it. For sake of illustration, we encircled two regions, one where there are AuNPs (continuous line) and another one where there is none (dashed line). While DF gives a similar intensity for both regions, TCDF, like TPL, enables a clear differentiation. This similarity can be quantified using the Pearson's correlation coefficient between the histograms of the normalized images. Figure 5G shows such calculation for 33 cells. Dashed lines correspond to mean values and coloured areas to standard deviation. It can be clearly seen correlation between TCDF and TPL is higher than between DF and TPL. This demonstrates that our approach, despite it simplicity, could be used as an alternative to TPL in order to monitor and track metal NPs in living cells.

Discussion and conclusions

In this work, the choice of gold nanorods (GNRs) was motivated by their unique combination of properties[13], including well-known synthesis, resonance tunability, as well as, flexible surface functionalization and biocompatibility. Nevertheless, TCDF can be easily extended to other optically resonant nanoparticles, with different sizes and shapes.

The election of the illumination colors depends solely on the scattering spectrum of the nanoparticles used, in such a way one of them must be on-resonance with the plasmon wavelength and the other must be off-resonance. Once the color-pair is established it is necessary to check the scattering ratio between the the two wavelengths remains constant for every part of the sample, and that the scattering response of the host is distinguishable from the one of the NPs (Supplementary Figure S8).

While data shown here are already very promising, it should be stressed that the method's performance could be further improved by optimizing the optical setup. For instance, by collecting the back-scattering instead of the forward-scattering, the contrast could be further increased, hence the sensitivity. While the absolute contrast enhancement and sensitivity depend on the specific optical setup and calibration algorithms, as well as the cell line / nanoparticle combination, our approach is potentially very general and transposable to a wide range of experimental implementations.

In spite of resonant metal NPs in cells can be accurately monitored using advanced microscopies as for instance two-photon luminescence (TPL) and SEM/TEM, these are slow, require complex and expensive equipment and are usually invasive. On the other hand, there are techniques that focus on high-throughput, like lens-free holography[57], but cannot be used for monitoring the cell-NPs interaction in a simple manner. In this paper, we have introduced an alternative optical technique that overcomes these limitations and proves to be efficient and versatile: It works for very different cell morphologies (adherent and suspension), measurement conditions (static and flowing) and purposes (fast screening and NPs tracking).

Although validated on AuNPs in cells, the technique could be easily generalized to any kind of NPs with resonant optical re-

Nanoscale Accepted Manuscript

This journal is © The Royal Society of Chemistry [year]

View Article Online
DOI: 10.1039/C7NR09408F

Published on 17 January 2018. Downloaded by University of Reading on 19/01/2018 20:21:25.

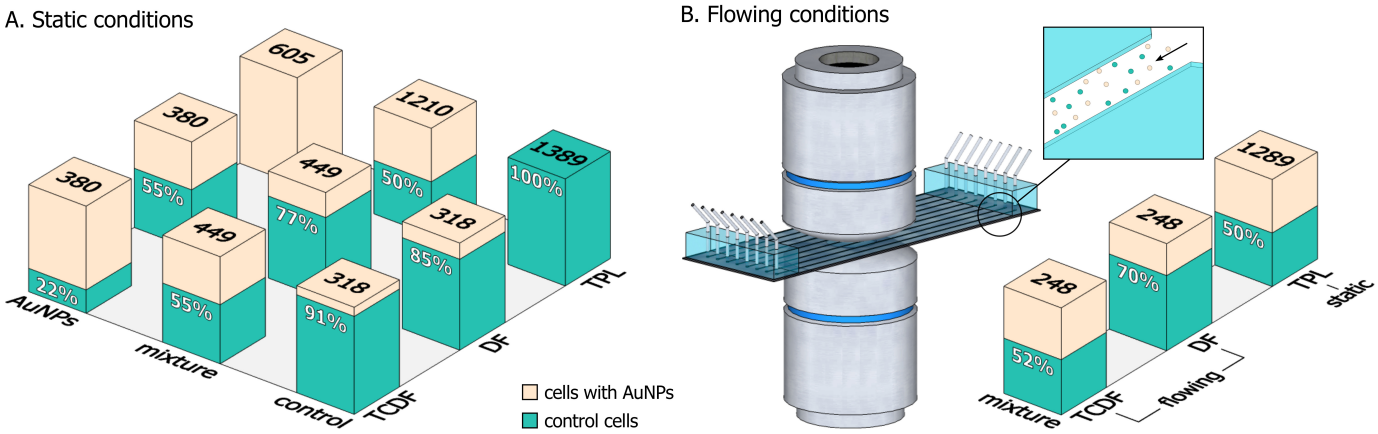

Fig. 4 Screening of AuNPs-loaded suspension cells under static (A) and flowing (B) conditions. Columns show classification of cells according to each method used for each sample. Percentages correspond to identified-as-control cells and the total number of cells analyzed is on top of each column. We identify the cells as with or without AuNPs depending of their intensity compared to an established threshold. For each method, we set the threshold using the expected value and standard deviation of the control sample cell's mean intensity distribution (Supplementary figure S4). **A.** We studied three samples: cells with no NPs (control), cells loaded with metal NPs (AuNPs) and a half-half combination of these (mixture). In the case of AuNPs and mixture samples, DF clearly underestimates the amount of cells loaded with AuNPs. On the contrary, TCDF measured values are much closer to the real ones. **B.** We studied mixture sample using DF and TCDF under flowing conditions and compare their results with TPL measurements under static conditions. It can be seen TCDF values are more similar to the actual values than DFs even under flowing conditions. We also present a sketch of the microfluidic chip between the condenser and microscope objective. Figure S5 in the supplementary information shows images of measured cells flowing through the channel.

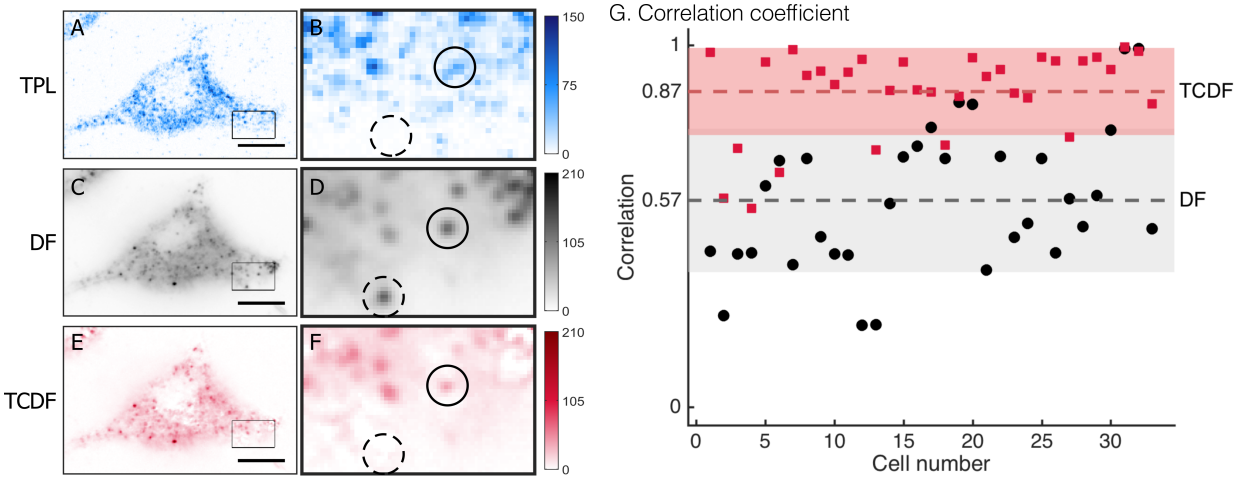

Fig. 5 High-resolution imaging of AuNPs in cells. Images of a complete cell (A, C, E) and a detail of it (B, D, F) using TPL (A, B), DF (C, D) and TCDF (E, F). Scale bar is 10 μm. Encircled regions show areas where there are AuNPs (continuous line) and where there are none (dashed line). Intensity difference between them is clear for TPL and TCDF, but it is not for DF. Graph G shows the Pearson's correlation coefficient between DF and TPL (black dots) and between TCDF and TPL (red squares). Correlation was computed using the histograms of the normalized images for 33 cells. Dashed lines represent mean values and colored areas the standard deviation. Here it is clear correlation between TCDF's images and TPL's is better than DF's.

Nanoscale Accepted Manuscript

View Article Online
DOI: 10.1039/C7NR09408F

Published on 17 January 2018. Downloaded by University of Reading on 19/01/2018 20:21:25.

sponse as well as other systems hosts, like bacteria and vesicles, or even non-biological specimens, provided the spectral response of the host significantly differs from the NPs one and the scattering intensity ratio is the same through all the sample for the two illumination wavelengths used.

Acknowledgments

V.R.F. and R.Q. acknowledge financial support from the Spanish Ministry of Economy and Competitiveness, through the "Severo Ochoa" Programme for Centres of Excellence in R&D (SEV-2015-0522), the Fundació Privada Cellex, and the CERCA Programme from the Generalitat de Catalunya. Authors thank Jordi Morales Dalmau for performing the scattering cross-section calculations, Jaime Ortega and Pascal Berto for fruitful discussions, as well as Clara Vilches and Merche Rivas for advice and help with cell culturing.

References

1 K. Riehemann, S. W. Schneider, T. A. Luger, B. Godin, M. Ferrari and H. Fuchs, *Angewandte Chemie International Edition*, 2009, **48**, 872–897.
2 T. L. Doane and C. Burda, *Chem. Soc. Rev.*, 2012, **41**, 2885–2911.
3 M. Medina-Sanchez, S. Miserere and A. Merkoci, *Lab Chip*, 2012, **12**, 1932–1943.
4 M. Holzinger, A. Le Goff and S. Cosnier, *Frontiers in Chemistry*, 2014, **2**, 63.
5 M. Ferrari, *Nat Rev Cancer*, 2005, **5**, 161–171.
6 R. Viswambari Devi, M. Doble and R. S. Verma, *Biosensors and Bioelectronics*, 2015, **68**, 688–698.
7 O. Veiseh, B. C. Tang, K. A. Whitehead, D. G. Anderson and R. Langer, *Nat Rev Drug Discov*, 2015, **14**, 45–57.
8 L. Y. Rizzo, B. Theek, G. Storm, F. Kiessling and T. Lammers, *Current Opinion in Biotechnology*, 2013, **24**, 1159–1166.
9 X. Xu, W. Ho, X. Zhang, N. Bertrand and O. Farokhzad, *Trends in Molecular Medicine*, 2015, **21**, 223–232.
10 L. C. Kennedy, L. R. Bickford, N. A. Lewinski, A. J. Coughlin, Y. Hu, E. S. Day, J. L. West and R. A. Drezek, *Small*, 2011, **7**, 169–183.
11 E. C. Dreaden, A. M. Alkilany, X. Huang, C. J. Murphy and M. A. El-Sayed, *Chem. Soc. Rev.*, 2012, **41**, 2740–2779.
12 X. Yang, M. Yang, B. Pang, M. Vara and Y. Xia, *Chemical Reviews*, 2015, **115**, 10410–10488.
13 P. K. Jain, K. S. Lee, I. H. El-Sayed and M. A. El-Sayed, *The Journal of Physical Chemistry B*, 2006, **110**, 7238–7248.
14 N. Khlebtsov and L. Dykman, *Chem. Soc. Rev.*, 2011, **40**, 1647–1671.
15 W. Zhou, X. Gao, D. Liu and X. Chen, *Chemical Reviews*, 2015, **115**, 10575–10636.
16 M. F. H. Carneiro and F. B. Jr., *Journal of Toxicology and Environmental Health, Part B*, 2016, **19**, 129–148.
17 J. Stone, S. Jackson and D. Wright, *Wiley Interdisciplinary Reviews: Nanomedicine and Nanobiotechnology*, 2011, **3**, 100–109.
18 A. E. Nel, L. Madler, D. Velegol, T. Xia, E. M. V. Hoek, P. Somasundaran, F. Klaessig, V. Castranova and M. Thompson, *Nat Mater*, 2009, **8**, 543–557.
19 R. Lévy, U. Shaheen, Y. Cesbron and V. Sée, *Nano Reviews*, 2010, **1**, 4889.
20 A. Albanese, P. S. Tang and W. C. Chan, *Annual Review of Biomedical Engineering*, 2012, **14**, 1–16.
21 L. A. Dykman and N. G. Khlebtsov, *Chemical Reviews*, 2014, **114**, 1258–1288.
22 L. Shang, K. Nienhaus and G. U. Nienhaus, *Journal of Nanobiotechnology*, 2014, **12**, 1–11.
23 T. L. Moore, L. Rodriguez-Lorenzo, V. Hirsch, S. Balog, D. Urban, C. Jud, B. Rothen-Rutishauser, M. Lattuada and A. Petri-Fink, *Chem. Soc. Rev.*, 2015, **44**, 6287–6305.
24 A. Verma and F. Stellacci, *Small*, 2010, **6**, 12–21.
25 E. C. Cho, Q. Zhang and Y. Xia, *Nat Nano*, 2011, **6**, 385–391.
26 J. A. Kim, C. Aberg, A. Salvati and K. A. Dawson, *Nat Nano*, 2012, **7**, 62–68.
27 B. D. Chithrani, A. A. Ghazani and W. C. W. Chan, *Nano Letters*, 2006, **6**, 662–668.
28 M. M. Mkandawire, M. Lakatos, A. Springer, A. Clemens, D. Appelhans, U. Krause-Buchholz, W. Pompe, G. Rodel and M. Mkandawire, *Nanoscale*, 2015, **7**, 10634–10640.
29 H. Wang, T. B. Huff, D. A. Zweifel, W. He, P. S. Low, A. Wei and J.-X. Cheng, *Proceedings of the National Academy of Sciences of the United States of America*, 2005, **102**, 15752–15756.
30 B. van den Broek, B. Ashcroft, T. H. Oosterkamp and J. van Noort, *Nano Letters*, 2013, **13**, 980–986.
31 I. H. El-Sayed, X. Huang and M. A. El-Sayed, *Nano Letters*, 2005, **5**, 829–834.
32 S. Patskovsky, E. Bergeron and M. Meunier, *Journal of Biophotonics*, 2015, **8**, 162–167.
33 X.-F. Jiang, Y. Pan, C. Jiang, T. Zhao, P. Yuan, T. Venkatesan and Q.-H. Xu, *The Journal of Physical Chemistry Letters*, 2013, **4**, 1634–1638.
34 T. Wang, D. Halaney, D. Ho, M. D. Feldman and T. E. Milner, *Biomedical Optics Express*, 2013, **4**, 584–595.
35 M. Kinnunen, A. V. Bykov, J. Tuorila, T. Haapalainen, A. V. Karmenyan and V. V. Tuchin, *Journal of Biomedical Optics*, 2014, **19**, 071409.
36 L. Wu and B. M. Reinhard, *Chemical Society Reviews*, 2014, **43**, 3884–3897.
37 J. R. Mourant, M. Canpolat, C. Brocker, O. Espondo-Ramos, T. M. M. A. Johnson, K. Stetter and J. P. Freyer, Proc. SPIE 3917, Optical Biopsy III, 2000, pp. 33–43.
38 R. A. Drezek, M. Guillaud, T. G. Collier, I. Boiko, A. Malpica, C. E. MacAulay, M. Follen and R. R. Richards-Kortum, *Journal of Biomedical Optics*, 2003, **8**, 7–16.
39 Y. Cui, X. Wang, W. Ren, J. Liu and J. Irudayaraj, *ACS Nano*, 2016, **10**, 3132–3143.
40 CytoViva, Inc., *http://cytoviva.com/products/hyperspectral-imaging-2/hyperspectral-imaging/*, accessed April 2017.
41 F. Xu, M. Reiser, X. Yu, S. Gummuluru, L. Wetzler and B. M. Reinhard, *ACS Nano*, 2016, **10**, 1189–1200.

Nanoscale Accepted Manuscript

This journal is © The Royal Society of Chemistry [year]

View Article Online
DOI: 10.1039/C7NR09408F

42 G. Rong, H. Wang, L. R. Skewis and B. M. Reinhard, *Nano Letters*, 2008, **8**, 3386–3393.

43 D. M. Wiener and T. A. Lionberger, *Analytical Chemistry*, 2013, **85**, 5095–5102.

44 G. Rong, H. Wang and B. M. Reinhard, *Nano Letters*, 2010, **10**, 230–238.

45 L. Novotny and B. Hecht, in *Principles of Nano-Optics*, Cambridge University Press, 2nd edn., 2012, ch. 12.

46 N. R. Jana, L. Gearheart and C. J. Murphy, *Advanced Materials*, 2001, **13**, 1389–1393.

47 B. Nikoobakht and M. A. El-Sayed, *Chemistry of Materials*, 2003, **15**, 1957–1962.

48 B. T. Draine and P. J. Flatau, *J. Opt. Soc. Am. A*, 1994, **11**, 1491–1499.

49 Arnida, A. Malugin and H. Ghandehari, *Journal of Applied Toxicology*, 2010, **30**, 212–217.

50 P. K. Jain, I. H. El-Sayed and M. A. El-Sayed, *Nano Today*, 2007, **2**, 18–29.

51 D. A. Giljohann, D. S. Seferos, W. L. Daniel, M. D. Massich, P. C. Patel and C. A. Mirkin, *Angewandte Chemie International Edition*, 2010, **49**, 3280–3294.

52 E. C. Wang and A. Z. Wang, *Integr. Biol.*, 2014, **6**, 9–26.

53 X. Zhe, M. L. Cher and R. D. Bonfil, *American journal of cancer research*, 2011, **1**, 740—751.

54 G. Liu, X. Mao, J. A. Phillips, H. Xu, W. Tan and L. Zeng, *Analytical Chemistry*, 2009, **81**, 10013–10018.

55 M. Maltez-da Costa, A. de la Escosura-Muñiz, C. Nogués, L. Barrios, E. Ibáñez and A. Merkoçi, *Nano Letters*, 2012, **12**, 4164–4171.

56 M. Perfezou, A. Turner and A. Merkoci, *Chemical Society Reviews*, 2012, **41**, 2606–2622.

57 Q. Wei, E. McLeod, H. Qi, Z. Wan, R. Sun and A. Ozcan, *Scientific Reports*, 2013, **3**, 1699 EP–.

Published on 17 January 2018. Downloaded by University of Reading on 19/01/2018 20:21:25.

Nanoscale Accepted Manuscript

Electronic Supplementary Material (ESI) for Nanoscale.
This journal is © The Royal Society of Chemistry 2018

Electronic supplementary information (ESI) to Two-Color Dark-Field (TCDF) microscopy for metal nanoparticles imaging inside cells

Valeria Rodríguez-Fajardo,[a,b] Vanesa Sanz,[a] Ignacio de Miguel,[a]
Johann Berthelot,[a‡] Srdjan S. Aćimović,[a§] Rafael Porcar-Guezenec,[b] and Romain Quidant*[a,c]

[a] *ICFO-Institut de Ciencies Fotoniques, The Barcelona Institute of Science and Technology, 08860 Castelldefels, Barcelona, Spain; E-mail: romain.quidant@icfo.eu*
[b] *COSINGO-Imagine Optic Spain S.L., Av. Canal Olimpic, s/n 08860 Castelldefels (Barcelona) Spain*
[c] *ICREA-Institució Catalana de Recerca i Estudis Avançats, 08010 Barcelona, Spain*
‡ *Present address: Aix Marseille Université, CNRS, Centrale Marseille, Institut Fresnel UMR 7249, 13397 Marseille, France*
§ *Present address: NIL Technology ApS, Diplomvej 381, DK-2800 Kongens Lyngby, Denmark*

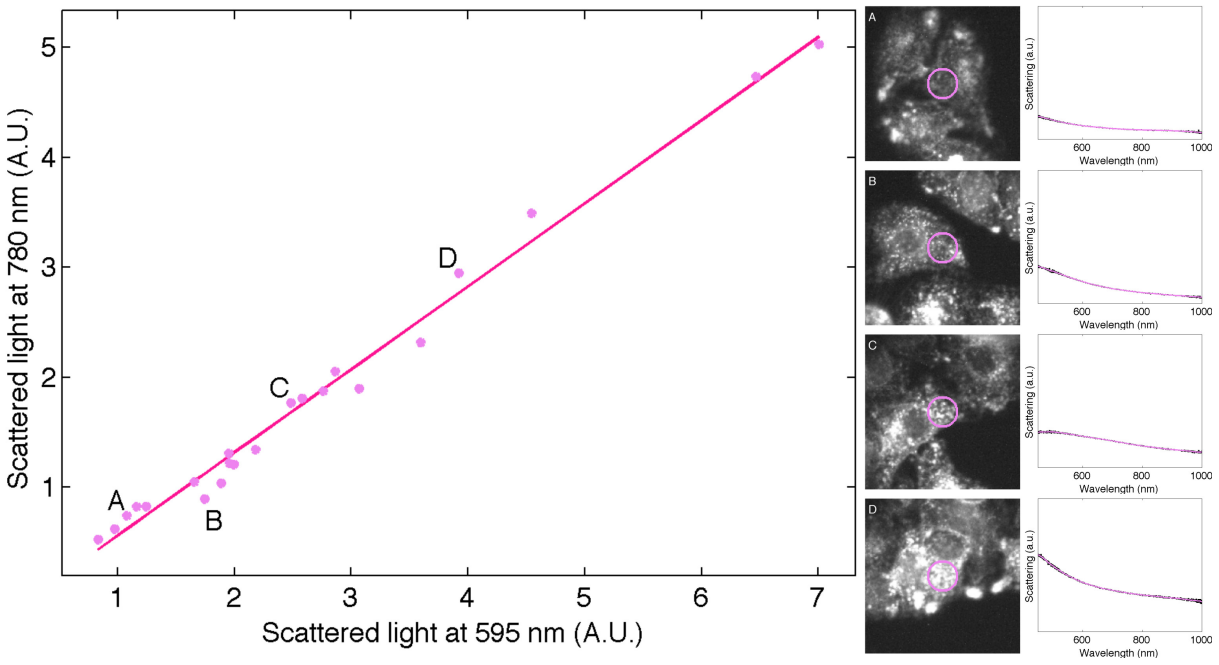

Figure S1: Scattering spectra of A495 cells and the relationship between scattered intensity at 780 nm and 595 nm. Intensities of scattered light from cells at 780 nm and 595 nm are not equal but they are related by a constant factor. This is crucial for our technique to work, as such a difference can be compensated simply by adjusting light sources intensity. Scattering spectra from cells were acquired for several cells and different organelles inside them. Graph shows data taken and linear fit, as well as four examples of the detection area in the cell and corresponding acquired spectrum.

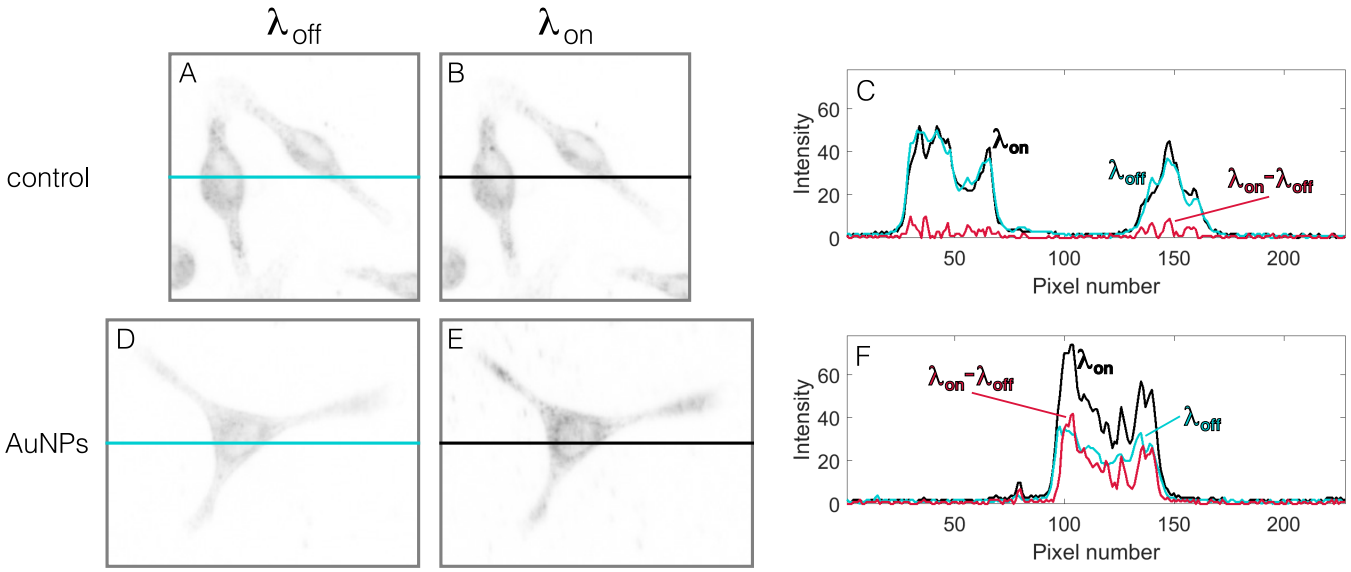

Figure S2: Images for each wavelength of cells presented in Figure 2. Images on-resonance (λ_{on}: B and E) correspond to DF images in Figure 2 (D and E, respectively). In spite of intensity of cells is very similar for control and AuNPs-loaded cells using DF microscopy (B vs. E), when comparing those to their off-resonance counterpart (λ_{off}: A and D), the presence of NPs becomes evident: intensity of images of control cell is very similar for both wavelengths (A vs. B), whereas it is not for AuNPs-loaded cell (D vs. E). Intensity profiles are also shown for control (C) and AuNPs-loaded (F) cells. Graph C exemplify how TCDF significantly reduces the scattering from the cell by subtracting the λ_{on} and λ_{off} images. Graph F illustrates how in the presence of NPs, such subtraction between the images, gives non-negligible signal. Although our method does not completely cancels the background, it is sufficient to carry out unequivocal discrimination between bare and loaded cells.

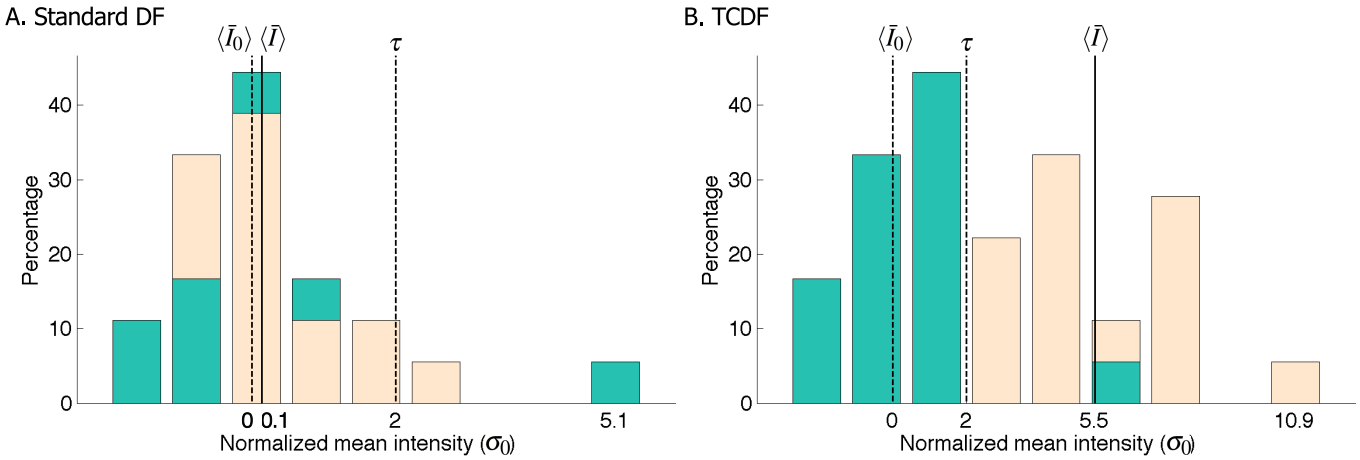

Figure S3: Distributions of cells mean intensity for control (green) and AuNPs-loaded (light orange) cells for A. standard DF and B. TCDF. Data shown correspond to 0 nm and 2 nM concentration of AuNPs during incubation, respectively, of one the experiment realizations. We normalized the data to the standard deviation of control distribution σ_0 and centered the data around the control sample average $\langle \bar{I}_0 \rangle$. We determine the threshold τ using only the data from the control sample as $\tau = \langle \bar{I}_0 \rangle + 2\sigma_0$. One can confidently state the cells in a sample were loaded with NPs if the contrast value ($C = \frac{\langle \bar{I} \rangle - \langle \bar{I}_0 \rangle}{\sigma_0}$) is greater than or equal to two; this is, if the average per sample ($\langle \bar{I} \rangle$) is separated from the average of control sample ($\langle \bar{I}_0 \rangle$) by more than twice the control sample's standard deviation (τ).

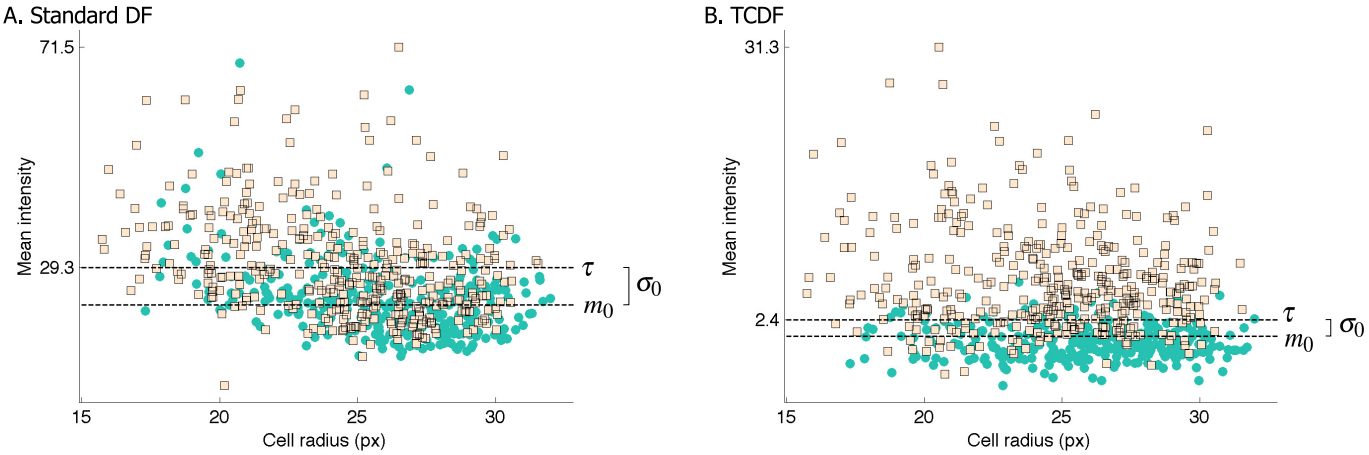

Figure S4: Scatter plots of cell's mean intensity and radius for control (green) and AuNPs-loaded (light orange) cells for A. standard DF and B. TCDF. Threshold τ was determined solely from data of the control sample as its mode value m_0 plus its standard deviation σ_0 ($\tau = m_0 + \sigma_0$). A cell was classified as control if its mean intensity value was below τ. Conversely, a cell was classified as loaded if its mean intensity value was above the threshold.

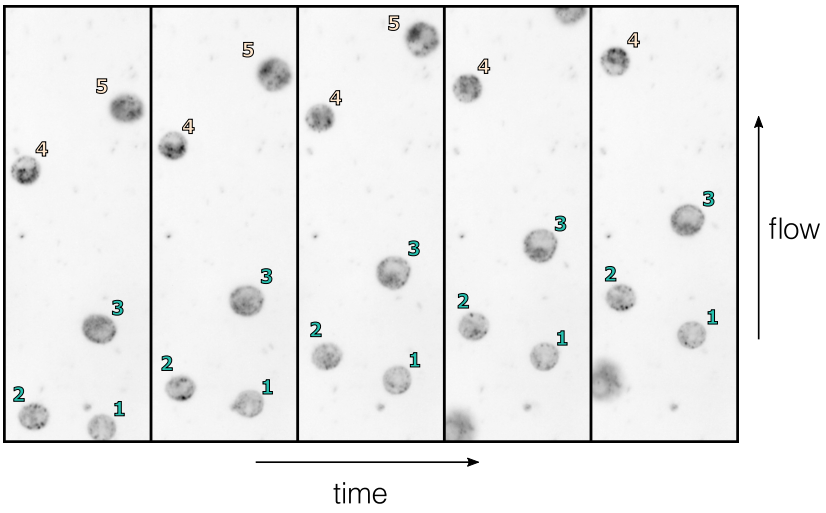

Figure S5: Example negative dark-field images of cells flowing through the microfluidic channel. Control and AuNPs-loaded cells are labeled with green and light orange numbers, respectively.

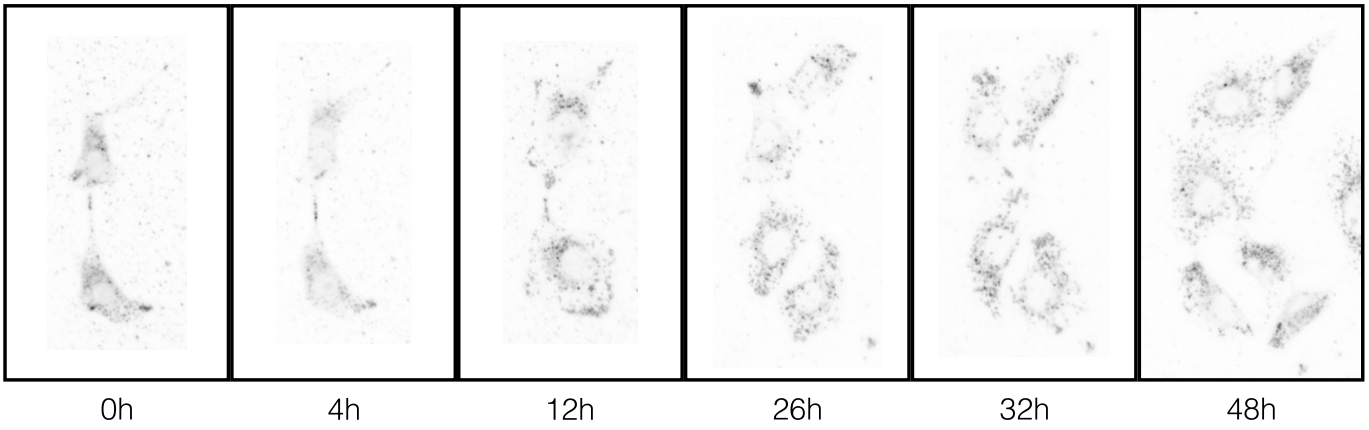

Figure S6: Dark-field negative images of a group of cells and their evolution over time. Dark-field illumination does not affect the cells health. Figure shows images of several AuNPs-loaded cells taken during 2 days. During data acquisition environment conditions for the cells were not controlled. Between each measurement cells were kept in the CO_2 incubator. It can be seen cells follow a normal trend for cell division, what implies their health is not compromised by the measurements.

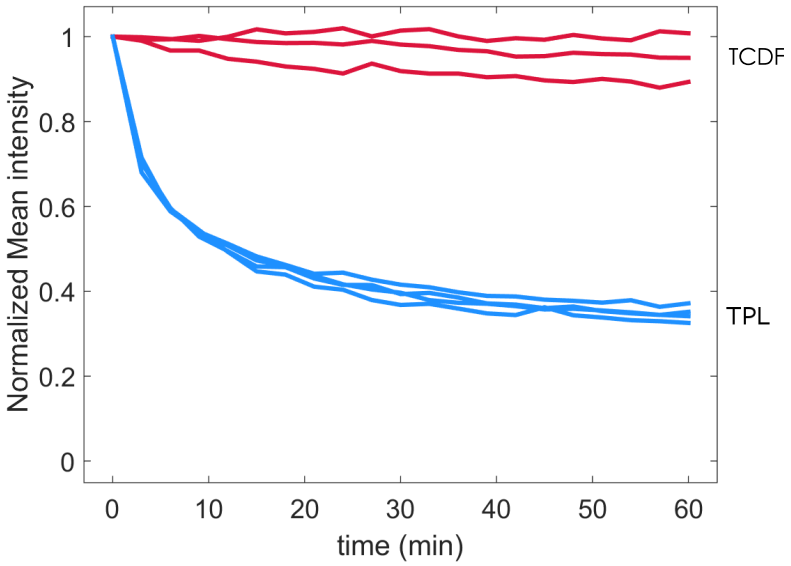

Figure S7: Mean intensity of TCDF and TPL along 1 hour. Metal nanoparticles are not affected by the scattering measurements. On the contrary, high peak intensities of TPL measurements can melt the nanoparticles, thus altering the signal intensity. This disadvantage of TPL can be overcome by decreasing the input laser intensity, but so does the signal collected, which in turn affects the method's sensitivity or time resolution.

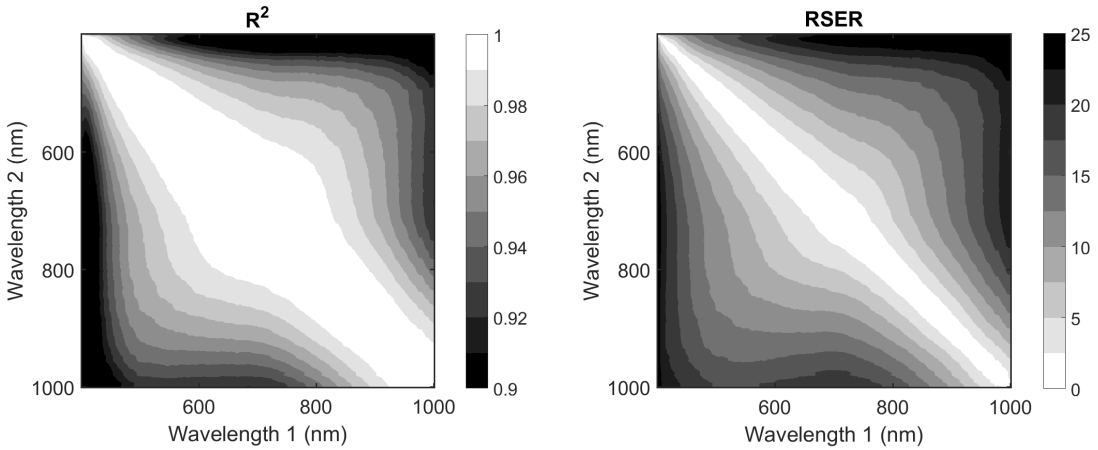

Figure S8: Evaluation of the fit goodness for different illumination wavelenght pairs. As for the case shown in figure S1, we fitted the scattering intensities for each wavelength pair using a linear model and evaluate how well this model fits the data. For this purpose, we used two parameters: the coefficient of determination ($R^2 = 1 - \left[\sum_{n=1}^{N}(y_n - f_n)^2\right] \Big/ \left[\sum_{n=1}^{N}(y_n - \bar{y})^2\right]$, with y_n is the value of the n-th data point, f_n its corresponding fitted value and $\bar{y}$ the data mean value) and the standard error of regression ($\text{SER} = \sqrt{\frac{1}{N-2}\sum_{n=1}^{N}(y_n - f_n)^2}$). The first one is a fairly common statistical value, that measures the percentage of the response variable variation, and it ranges from 0 to 1. The second one represents the average distance that the observed values fall from the regression line and uses the units of the response variable. Importantly, for a perfect fit $R^2 = 1$ and $\text{SER} = 0$. Since units for SER are different for each color pair, in order to compare how good are the fits, it is necessary to normalize it, therefore we defined $\text{RSER} = 100\frac{\text{SER}}{\bar{y}}$. Most R^2 values are above 0.9, which indicates the linear model describes well the data. This is reinforced by the parameter RSER, that for the major part of the analysed wavelength range is below 20%. In both cases the diagonal values correspond to a perfect fit, as expected considering in this case the wavelengths are equal. Although this case is not suitable for TCDF, it is useful to check the calculations. Ranges found for both R^2 and RSER demonstrate data fits well to a linear model for a broad range of wavelengths, therefore revealing TCDF would work for different illumination wavelength pairs, not only for the one we implemented.